



## Original Articles

## rsHRF: A toolbox for resting-state HRF estimation and deconvolution

Guo-Rong Wu<sup>a,b,1,\*</sup>, Nigel Colenbier<sup>b,c,d,1</sup>, Sofie Van Den Bossche<sup>b</sup>, Kenzo Clauw<sup>b</sup>,  
Amogh Johri<sup>e</sup>, Madhur Tandon<sup>f</sup>, Daniele Marinazzo<sup>b,d</sup>

<sup>a</sup> Key Laboratory of Cognition and Personality, Faculty of Psychology, Southwest University, Chongqing 400715, China

<sup>b</sup> Department of Data Analysis, Faculty of Psychology and Educational Sciences, Ghent University, Ghent 9000, Belgium

<sup>c</sup> Research Center for Motor Control and Neuroplasticity, KU Leuven, Leuven 3001, Belgium

<sup>d</sup> Brain Imaging and Neural Dynamics Research Group, IRCCS San Camillo Hospital, Venice 30126, Italy

<sup>e</sup> International Institute of Information Technology, Bangalore 560100, India

<sup>f</sup> Indraprastha Institute of Information Technology, Delhi 110020, India



## ARTICLE INFO

## Keywords:

resting-state fMRI  
HRF  
deconvolution  
brain connectivity  
MATLAB  
Python  
BIDS

## ABSTRACT

The hemodynamic response function (HRF) greatly influences the intra- and inter-subject variability of brain activation and connectivity, and might confound the estimation of temporal precedence in connectivity analyses, making its estimation necessary for a correct interpretation of neuroimaging studies. Additionally, the HRF shape itself is a useful local measure. However, most algorithms for HRF estimation are specific for task-related fMRI data, and only a few can be directly applied to resting-state protocols. Here we introduce rsHRF, a Matlab and Python toolbox that implements HRF estimation and deconvolution from the resting-state BOLD signal. We first provide an overview of the main algorithm, practical implementations, and then demonstrate the feasibility and usefulness of rsHRF by validation experiments with a publicly available resting-state fMRI dataset. We also provide tools for statistical analyses and visualization. We believe that this toolbox may significantly contribute to a better analysis and understanding of the components and variability of BOLD signals.

## 1. Introduction

An increasing number of studies investigate spontaneous blood oxygenation level-dependent (BOLD) fluctuations (Seeley et al., 2007; Zhang and Raichle, 2010). Most of these studies look at well-reproducible intrinsic-connectivity networks (ICNs) emerging from these resting-state recordings. These ICNs have been related to perception, emotion and cognitive functions in different populations, indicating a fundamental role for spontaneous BOLD fluctuations in understanding behaviour and clinical diseases (Zhang and Raichle, 2010; Laird et al., 2011). However, the BOLD signal is modulated by the cerebrovascular reactivity and neurovascular coupling, rather than a direct measure of neural activity. Thus, the interpretation of BOLD signals is not always straightforward. The cerebral blood flow (CBF), cerebral blood volume (CBV), and the cerebral metabolic rate of oxygen (CMRO<sub>2</sub>) have been considered as the primary contributors to BOLD signal changes in the previous biophysical models (e.g., Balloon model) of the cerebrovascular contribution to BOLD signal (Buxton et al., 1998; Friston et al., 2000; Buxton, 2012).

An electrophysiological validation study showed that the underlying neural connectivity (in terms of lagged directional statistical de-

pendencies) could be better recovered from deconvolved BOLD signals (David et al., 2008). This reveals that the variability of the hemodynamic response, as a function of changes in CBF, CBV and CMRO<sub>2</sub>, will give rise to spurious connectivity inference. It is still a challenge to distinguish differences due to modulations in neural activity from differences due to modulations in the hemodynamic response in empirical BOLD fMRI studies (Handwerker et al., 2012). Uncovering hemodynamic correlates of spontaneous neural activity is therefore quite important before mapping brain connectivity, as it might elucidate the underlying mechanisms that drive resting-state fMRI (rs-fMRI) dynamics (Keles et al., 2016).

The hemodynamic response function (HRF) has been shown to vary in timing, amplitude, and shape across brain regions, cognitive task paradigms, ageing and pathological populations (Miezin et al., 2000; Handwerker et al., 2012; Badillo et al., 2013). Such variation is expected also for resting state. However, the timing information of spontaneous events for HRF estimation cannot be easily identified without simultaneous electrophysiological recordings. Recent evidence demonstrated that ICNs can be recovered with only few infra-slow BOLD events, which are identified from the relatively large amplitude BOLD signal peaks (Tagliazucchi et al., 2012). The idea of events driving the BOLD signal

\* Corresponding author at: Key Laboratory of Cognition and Personality, Faculty of Psychology, Southwest University, Chongqing 400715, China.

E-mail address: [guorongwu@swu.edu.cn](mailto:guorongwu@swu.edu.cn) (G.-R. Wu).

<sup>1</sup> These authors contributed equally to this work.

has also been used in deconvolution approaches (Karahanoglu et al., 2013; Caballero-Gaudes et al., 2019) to disentangle activity related events. Using a point process approach to identify these events, our previous study provided a simple way for resting-state HRF estimation and deconvolution (Wu et al., 2013). The original idea was to improve the estimation of statistical dependencies between time series, which were proven to be confounded by the HRF also for non-lagged measures (Rangaprakash et al., 2018). In following studies, the retrieved resting-state HRF has been proposed as a useful biomarker for pharmacological and pathologically induced loss of consciousness, chronic pain, heart rate variability, post-traumatic stress disorder, and autism (Wu and Marinazzo, 2015, 2016; Rangaprakash et al., 2017; Yan et al., 2018; Wu et al., 2019).

The present study aims to present an open-source Python/Matlab toolbox for resting-state HRF deconvolution and brain connectivity analysis. We will first describe the principles of the blind HRF deconvolution algorithm implemented, and then validate it by a co-localized local field potentials (LFP) and intrinsic optical signals (IOS), which were simultaneously recorded from the rat primary somatosensory area (SI) under burst-suppression anaesthesia condition. Usage and utility of the methods provided by the toolbox is then demonstrated on publicly released resting-state fMRI datasets.

## 2. Materials and methods

### 2.1. Resting-state HRF estimation and deconvolution algorithm

We assume that resting-state BOLD fluctuations are driven by spontaneous neural events and that the corresponding BOLD events can be identified by point process analysis (Wu et al., 2013b). A linear time invariant (LTI) system is used to model the relationship between the spontaneous neural event and the BOLD response (Boynton et al., 2012). The hemodynamic response  $h(t)$  represents such dynamic process; the resting-state BOLD signal in a given voxel (or region) at time  $t$ ,  $y(t)$ , satisfies the following equation:

$$y(t) = \sum_{i=1}^M h(i)s(t-i) + \varepsilon(t), \varepsilon \sim N(0, \sigma^2 V) \quad (1)$$

where  $h(t)$  is the unknown hemodynamic response,  $\varepsilon$  is the measurement noise which is uncorrelated with the unknown spontaneous neural activity  $s(t)$ ,  $\sigma^2$  is the error variance,  $V$  is the error correlation matrix, obtained via an AR model and covariance across the regressors for each voxel, and  $M$  is the number of time bins spanning the desired length of the estimated HRF.

In order to solve Eq. (1) for  $h(t)$ , we substitute  $s(t)$  with a hypothetical model of the neural activation that we call  $\hat{s}(t)$ . Here we assume  $s(t) \approx \hat{s}(t - \tau)$ , where  $\hat{s}(t)$  is constituted by several time-shifted delta functions, which are centered at the onset of each spontaneous BOLD event, and  $\tau$  is a temporal deviation. As the peak of the BOLD signal lags behind the peak of neural activation (i.e.,  $k$  seconds), it is reasonable to assume that larger BOLD spikes are generated from spontaneous neural events. This enables us to retrieve the timing information of these spontaneous neural events.

The time lag  $k$  (corresponding to the best estimate of  $\tau$ ), and the HRF  $h$  can be simultaneously obtained by minimizing the least square error associated with Eq. (1) (Wu et al., 2013b; Wu and Marinazzo, 2016), i.e. the optimization problem:

$$\hat{h}, \hat{k} = \arg \left\| y(t) - \sum_{i=1}^M h(i)\hat{s}(t-i) \right\| \quad (2)$$

$$\hat{s}(t-k) = \begin{cases} 1, & t \in ST \\ 0, & t \notin ST \end{cases}, 0 < k \leq PT$$

where  $\|\cdot\|$  is the  $L_2$  norm,  $PT$  is the peri-event time. In practice, the timing set  $ST$  of these resting-state BOLD spikes/transients is defined as the time points for which the BOLD signal exceeds a given threshold

$\lambda$ . This set can be obtained using the following rule:

$$ST\{i\} = t_i, y(t_i) \geq \lambda \text{ \& } y(t_i) \geq y(t_i \pm j). \quad (3)$$

So  $\hat{ST} = ST - \hat{k} = \{t_i - \hat{k}\}$  indicates the most likely onset time point of the spontaneous neural event, and  $j$  indicates the desired width of the peak (in bins) in order to characterize the local maximum. A temporal mask is always added to exclude pseudo point process events induced by motion artefacts.

To characterize the shape of the hemodynamic response, three parameters of the HRF, namely response height (RH), time to peak (TTP), and Full Width at Half Maximum (FWHM), are estimated. These quantities are interpretable in terms of potential proxies for response magnitude, latency, and duration of neuronal activity (Lindquist and Wager 2007).

The estimated spontaneous neural activity  $\hat{s}(t)$  was then derived using Wiener deconvolution:

$$G(f) = H^*(f)S(f)[|H(f)|^2S(f) + N(f)]^{-1}, \quad (4)$$

$$\hat{s}(t) = \mathcal{F}^{-1}\{G(f)Y(f)\}, \quad (5)$$

where  $\mathcal{F}^{-1}$  is the inverse Fourier transform operator,  $*$  denotes complex conjugate,  $S(f) = E|X(f)|^2$  and  $N(f) = E|V(f)|^2$  are the mean power spectral density of  $s(t)$  and  $\varepsilon(t)$  respectively.  $H(f)$ ,  $X(f)$ ,  $Y(f)$  and  $V(f)$  are the Fourier transform of  $h(t)$ ,  $s(t)$ ,  $y(t)$  and  $\varepsilon(t)$ . The  $N(f)$  is typically unknown in practice, but can be reliably estimated based on the median estimator on the finest scale wavelet coefficients of  $y(t)$  (Neelamani et al., 2004). The iterative Wiener filter algorithm was further conducted to restore  $\hat{s}(t)$  (Hiller and Chin 1991). The pseudo-code of iterative algorithm can be summarized as follows:

$$S_0(f) = E|Y(f)|^2$$

FOR  $i = 1$  to  $n$

$$G_i(f) = H^*(f)S_{i-1}(f)[|H(f)|^2S_{i-1}(f) + N(f)]^{-1}$$

$$X_i(f) = G_i(f)Y(f),$$

$$S_i(f) = E|X_i(f)|^2 + S_{i-1}(f)N(f)[|H(f)|^2S_{i-1}(f) + N(f)]^{-1}$$

END FOR

$$\hat{s}(t) = \mathcal{F}^{-1}\{G_n(f)Y(f)\}$$

In the loop above,  $n$  is the maximum number of iterations. When the  $\|S_i(f) - S_{i-1}(f)\|$  function reaches a knee, the iteration stops.

### 2.2. rsHRF implementations

The original code of resting-state HRF deconvolution was firstly written and developed in Matlab (Wu et al., 2013b). Currently, the updated versions to perform these analyses (through Matlab, Python, Docker, and BIDS-App) are freely accessible from the NITRC page: <https://www.nitrc.org/projects/rsHRF>. More detailed information along with a toolbox manual are provided in the toolbox and on the NITRC page.

The current version of the Matlab toolbox (version 2.4) provides an extension of SPM, consisting of four main parts: (1) denoising; (2) HRF estimation and deconvolution; (3) HRF viewer; (4) brain connectivity (for a schematic overview; see Fig. 1).

The python version consists of the HRF estimation and deconvolution part only, both as command line interface, and as graphical user interface. The Python command line interface parameters is shown in Table S1.

Prior to rsHRF analysis, the data should be already pre-processed, such as realignment for resting-state BOLD fMRI data. rsHRF provides several signal denoise options: nuisance regression, temporal filtering

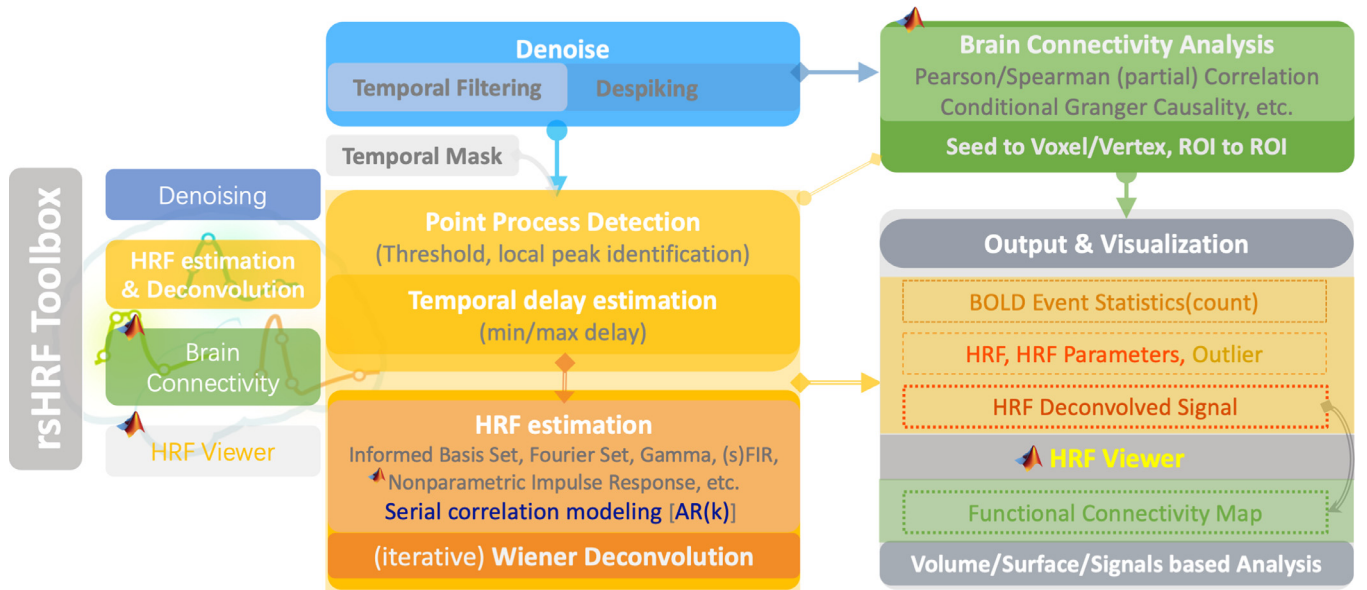


Fig. 1. Workflow of the rsHRF toolbox.

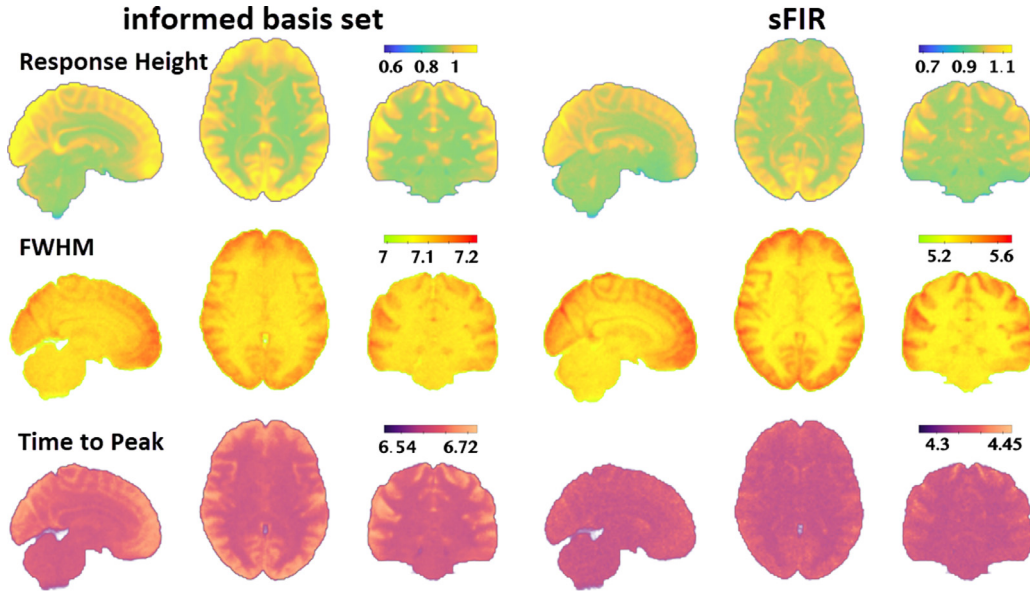


Fig. 2. Mean spatial distribution maps for the HRF parameters estimated using an informed basis set (left) and the sFIR algorithm (right).

and despiking. The input data could be 3D volume (Nifti), 2D surface (GIFTI), or text, or .mat file, in native or MNI space (only for Nifti/GIFTI data).

HRF estimation and deconvolution will be performed after several necessary parameter configuration: HRF basis function (including: informed basis function, Gamma functions, Fourier set (Hanning), (smooth) Finite impulse response, nonparametric impulse response); duration of HRF ( $PT$ ); minimum/maximum time delay ( $k$ ); microtime resolution for onset estimation; serial correlation model (AR); threshold for point process detection ( $\lambda$ ); temporal mask to exclude spurious events; HRF deconvolution algorithms (e.g. Wiener filter). rsHRF output includes the number of events, HRF parameters (RH, TTP, FWHM), deconvolved data. A simple demo script is shown in Table 1. The outlier detection and replacement procedure can be performed on HRF parameters and deconvolved data for 3D volume images.

It is worth stressing that the shape parameters are retrieved after the HRF estimation and are not part of the estimation procedure itself.

Seed to voxel or ROI (region of interest) to ROI functional connectivity (FC) analysis can be further implemented based on the data

with or without deconvolution. There are two ways for ROI setting, (1) sphere definition based on the coordinates, (2) atlas. Several functional connectivity measures are provided in rsHRF Matlab toolbox, (1) Pearson/Spearman (partial) correlation, (2) pairwise/partially conditioned/conditioned Granger causality (Marinazzo et al., 2012; Wu et al., 2013a,b).

### 2.3. rsHRF development

To facilitate running and testing rsHRF with continuous integration, we feature a unit testing framework for all HRF estimation algorithms and iterative Wiener deconvolution, both in Matlab and Python.

### 2.4. Compatibility and interoperability

Both as a SPM extension, and as a Python BIDS-App, the toolbox is compatible with data organized according to the Brain Imaging Data Structure (BIDS). As such it is fully modular and can be inserted in an

**Table 1**

An example set of commands for resting-state HRF estimation in Matlab and Python.

Matlab Code	Python Code
<pre>%basis function para.name = 'Gamma functions';  % number of basis functions para.order = 3; %TR=2 s para.TR = 2; %Microtime resolution = TR/3 s para.T = 3; para.T0=1;para.dt = para.TR/para.T;  %AR(1) noise autocorrelation. para.AR_lag = 1; % (mean + para.thr*standard deviation) threshold to detect event. para.thr = 1; % length of HRF, in seconds para.len = 24; % minimum/maximum delay allowed between event and HRF onset (seconds) mint = 4; maxt = 8; para.lag = fix(mint/para.dt):fix(maxt/para.dt);  % temporal mask, no event was excluded Tmask = []; % HRF estimation [beta_hrf, bf, event_bold] = rsHRF_estimation_temporal_basis(boldsig,para,Tmask); % estimated HRF HRF = bf*beta_hrf(1:size(bf,2),:);</pre>	<pre>import numpy as np from rsHRF import spm_dep, utils, basis_functions para = {} para['estimation'] = 'gamma'  para['order'] = 3  para['TR'] = 2  para['T'] = 3; para['T0'] = 1; para['dt'] = para['TR']/para['T']  para['AR_lag'] = 1  para['thr'] = 1  para['len'] = 24  para['min_onset_search'] = 4, para['max_onset_search'] = 8 para['lag'] = np.arange(np.fix(para['min_onset_search'] / para['dt']), np.fix(para['max_onset_search'] / para['dt']) + 1, dtype='int')  Tmask=[]  bf = basis_functions.basis_functions.get_basis_function(bold_sig.shape, para) beta_hrf, event_bold = utils.hrf_estimation.compute_hrf(data, para, Tmask, 1, bf=bf)  HRF = np.dot(bf, beta_hrf[np.arange(0, bf.shape[1]),:])</pre>

analysis pipeline (typically after the preprocessing steps). The toolbox can also be run on the cloud thanks to the inclusion in brainlife.io.

## 2.5. Datasets and analyses

### 2.5.1. Simultaneous IOS and LFP recording from a Sprague-Dawley rat

The spontaneous LFP and IOS in SI were simultaneously recorded from a Sprague-Dawley rat (male) under 1.8–2% isoflurane anesthesia, which was detailed described in (Pan et al., 2018). In the current study, we used the optical recording measured at 525 nm.

The physiological pulses of respiratory and cardiac rates in the IOS were removed with notch-filters. The envelope of 1–100 Hz LFP amplitudes were obtained using the Hilbert transform. Before HRF estimation, both IOS and LFP envelope were detrended and down-sampled to 1 and 0.5 Hz, and the IOS was further temporally band-pass filtered (0.01–0.1Hz). The HRFs estimated with the LFP envelope or the point process of the LFP envelope (LFP<sub>pp</sub>) as input acted as the ground truth; we denote them as HRF<sub>LFP</sub> and HRF<sub>LFP-pp</sub> respectively. Here LFP<sub>pp</sub> is constituted by the time-shifted delta functions. The HRFs blindly estimated from the IOS data are denoted by HRF<sub>blind</sub>. To explore whether RH changes in blindly estimated HRF (HRF<sub>blind</sub>) is proportional to RH changes in measured HRF, we estimated HRF within a sliding window of  $L$  seconds ( $L = 150, 160, \dots, 230, 240$ ). Successive windows were shifted by 4 s (see *rsHRF\_demo\_LFP\_IOS.m* for details).

### 2.5.2. Resting-state fMRI dataset (Human Connectome Project)

The first resting-state fMRI dataset used here as an example is the Human Connectome Project (Van Essen et al., 2013). The rsHRF was retrieved from resting state scans of 878 subjects, taken from the minimally processed dataset, both in grey and white matter. The resulting maps have been uploaded on neurovault (<https://neurovault.org/collections/9465/>) and can be found on figshare too: ([https://figshare.com/articles/voxelwise\\_resting\\_state\\_HRF\\_shape\\_WM\\_and\\_GM\\_/7139702](https://figshare.com/articles/voxelwise_resting_state_HRF_shape_WM_and_GM_/7139702)). Here we report an representative figure (Figure 2), in which the different shape in grey and white matter is evident.

### 2.5.3. Resting-state fMRI dataset (UCLA Consortium for Neuropsychiatric Phenomics)

The second resting-state fMRI dataset used in this study has been publicly released by the UCLA Consortium for Neuropsychiatric Phenomics (Poldrack et al., 2016), consisting of both healthy individuals (130 subjects) and individuals with neuropsychiatric disorders including schizophrenia (50 subjects), bipolar disorder (49 subjects), and attention deficit/hyperactivity disorder (ADHD, 43 subjects). For both healthy and patient groups, participants were aged between 21 and 50 years. The resting-state fMRI data were collected on two 3T Siemens Trio scanners using a T2\*-weighted EPI sequence with the following parameters: TR=2s, TE=30 ms, flip angle=90°, matrix 64 × 64, FOV=192 mm, slice thickness=4 mm, 34 slices, duration=304 s.

The dataset has been pre-processed using the fMRIPrep pipeline (Gorgolewski et al., 2017), and can be accessed at <https://www.openfmri.org/dataset/ds000030/>. Seventy subjects with mean framewise displacement (FD) > 0.2 were excluded for further analysis. Afterwards, several confounding variables were regressed out from the volume/surface based BOLD signals: (1) six motion artefact parameters and their temporal derivatives, (2) non-neuronal sources of noise estimated using two separate approaches by the anatomical component correction method: (a) top six principal components from subject-specific white matter and cerebrospinal fluid mask (for surface based BOLD signal analysis), (b) top five principal components from subject-specific cerebrospinal fluid mask (for white matter BOLD signal analysis), and (3) the first-order Legendre polynomial. Then the residual time series were temporally band-pass filtered (0.01–0.1Hz), and despiked with a hyperbolic tangent squashing function. Finally, the data were blindly deconvolved using the hemodynamic deconvolution algorithm, with Gamma functions / Fourier set as the basis functions (see *rsHRF\_demo\_UCLA\_batch.m* for details).

### 2.5.4. Voxelwise/ROIwise HRF analysis

Statistical inference on the voxelwise white matter HRF was performed with a multivariate analysis program 3dMVM in AFNI



**Table 2**

Averaged Pearson correlation coefficients (with standard deviation) among the amplitudes of HRF across different size of sliding windows. Each Pearson correlation coefficient was calculated based on the RHs obtained from a sliding window of  $L$  seconds ( $L = 150, 160, \dots, 230, 240$ ).

$r$	TR=1 s	TR=2 s
HRF <sub>blind</sub> vs. HRF <sub>LFP-pp</sub>	0.55(0.11)	0.59 (0.05)
HRF <sub>blind</sub> vs. HRF <sub>LFP</sub>	0.82(0.04)	0.79 (0.04)
HRF <sub>LFP</sub> vs. HRF <sub>LFP-pp</sub>	0.60(0.19)	0.62(0.04)

(Chen et al., 2015). We applied 3dMVM on the smoothed HRF parameters (6 mm Gaussian kernel), with HRF parameters (RH, FWHM, TTP) as the within-subjects factor, and the group as a between-subjects factor (healthy controls, schizophrenia, bipolar disorder, ADHD), age, gender, scanner and mean FD as the covariates. Type I error due to multiple comparisons across voxels was controlled by false discovery rate (FDR) at voxel level. Statistical significance for group analysis was set at  $p_{FDR} < 0.05$ .

The surface-based ROIwise HRF was estimated using the Yeo 7-network parcellation (Yeo et al., 2011). The Matlab code of multivariate analysis of variance (*manova.m*) was employed as an alternative way for statistical analysis of HRF parameters. There are four different methods provided in *manova.m*: Wilks' lambda, Pillai's trace, Hotelling-Lawley trace, Roy's maximum root statistic. Here we only report results from Roy's maximum root statistic.

### 2.5.5. Brain connectivity analysis and connectome-based predictive modelling

The cross-sectional studies have indicated that age can be predicted from the FC of ICNs. A longitudinal study further demonstrated that default mode network (DMN) play an important role in aging (Ng et al., 2016). Here, we predict the individual age difference on healthy subjects from the FC of DMN. The coordinates of 9 ROIs (sphere of 6 mm radius) from the DMN were adopted from Raichle (2011) (see supporting material Table S2). FC was computed among 9 ROIs using partial Pearson's correlation. For comparison, ROI-to-ROI FC analyses were performed both on the signals with and without hemodynamic deconvolution.

Briefly, we employ relevance vector regression (RVR) algorithm to generate a predictive model of the age from FC matrices (Tipping, 2001), with gender, and mean FD as covariates, implementing in the PRoNto toolbox (<http://www.mlnl.cs.ucl.ac.uk/pronto/>). The leave one out cross-validation was used to evaluate the performance of RVR algorithm. The Pearson correlation coefficient ( $r$ ) and mean absolute error (MAE) were calculated between the actual and the predicted age for the overall model performance. The statistical significance of model performance was assessed by permutation test. As the rsfMRI datasets were collected from two scanners, we applied RVR model on two datasets separately. To assess the generalizability of the predictive model, we take one dataset as training data and another one as the test dataset.

## 3. Results

### 3.1. Simultaneous IOS and LFP recording

HRFs were estimated based on the finite impulse response (FIR) model. Fig. 3 displays the HRFs with TR=1s (HRFs with TR=2s are similar). Regardless of scale factor, the temporal profile of HRF<sub>blind</sub> exhibits a large overlap with the temporal profile of HRF<sub>LFP-pp</sub>, even when only parts of the data are used (Fig. 3B). Moreover, the amplitudes of the blindly estimated HRF (HRF<sub>blind</sub>) are positively correlated with the ones of the ground truth (HRF<sub>LFP</sub> or HRF<sub>LFP-pp</sub>), using different TRs (Table 2). The Pearson correlation coefficient of HRF parameters between the blindly estimated HRF and the ground truth is higher for HRF<sub>LFP</sub> than HRF<sub>LFP-pp</sub>. Nonetheless, the response height (RH) of HRF<sub>LFP-pp</sub> is proportional to the RH of HRF<sub>LFP</sub>, which indicates that

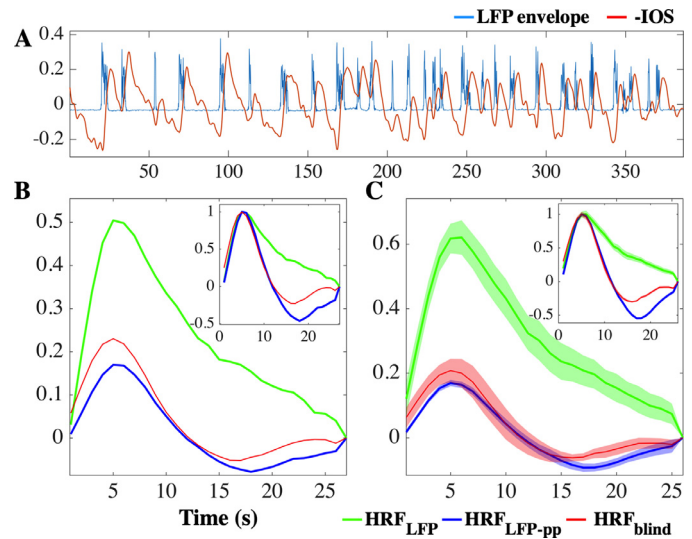


**Fig. 3.** (A) LFP envelope and IOS data. HRFs (HRF<sub>LFP</sub>, HRF<sub>LFP-pp</sub>, and HRF<sub>blind</sub>) retrieved from the whole data (B) and averaged HRFs across sliding windows of 200s (C, mean (solid line) + standard deviation (shadow)). The smaller panels within B and C display peak normalized HRFs.

the temporal information of LFP envelope signals can be represented as point processes.

### 3.2. Group HRF differences

In the white matter HRF analysis, the statistical maps of HRF parameters reveal that resting-state HRF varied across four groups (Fig. 4A). There was a main effect of group in the genu of corpus callosum and anterior corona radiata ( $p < 0.05$ , FDR corrected). The post-hoc analysis was further demonstrated in the supplementary material (Fig. S1). Finally, the HRF viewer was provided to visualize the HRF shape differences in voxel/ROI level (Fig. 4B).

For ROIwise analysis, the Roy's maximum root statistic indicated that the significant main effect of group was identified in dorsal attention and frontoparietal network ( $p < 0.05$ , FDR corrected). However, no significant result was found in post-hoc analysis without a priori comparisons.

### 3.3. Effects of HRF deconvolution on connectome-based prediction

The RVR algorithm could reliably predict age from FCs estimated from BOLD signal with and without hemodynamic deconvolution (Table 3). We found model performance and generalization are improved when using the BOLD signal was deconvolved.

### 3.4. Comparing results between matlab and python

The results are virtually the same (pointwise Pearson correlation between HRF shape greater than 0.99999), for all the estimation types (supplementary Fig. S2), checked with the compare.py script in the Python repository [https://github.com/BIDS-Apps/rsHRF/tree/master/consistency\\_test](https://github.com/BIDS-Apps/rsHRF/tree/master/consistency_test).

## 4. Computational cost

To quantify the computational cost, we report the running time of seven HRF estimation algorithms by running each algorithm with the parameters in Table 1 on a single core of the same computer (listed in Table 4). The toolbox was tested on a surface data (sub-10171\_task-rest\_bold\_space-fsaverage5.L.func.gii, which is available at

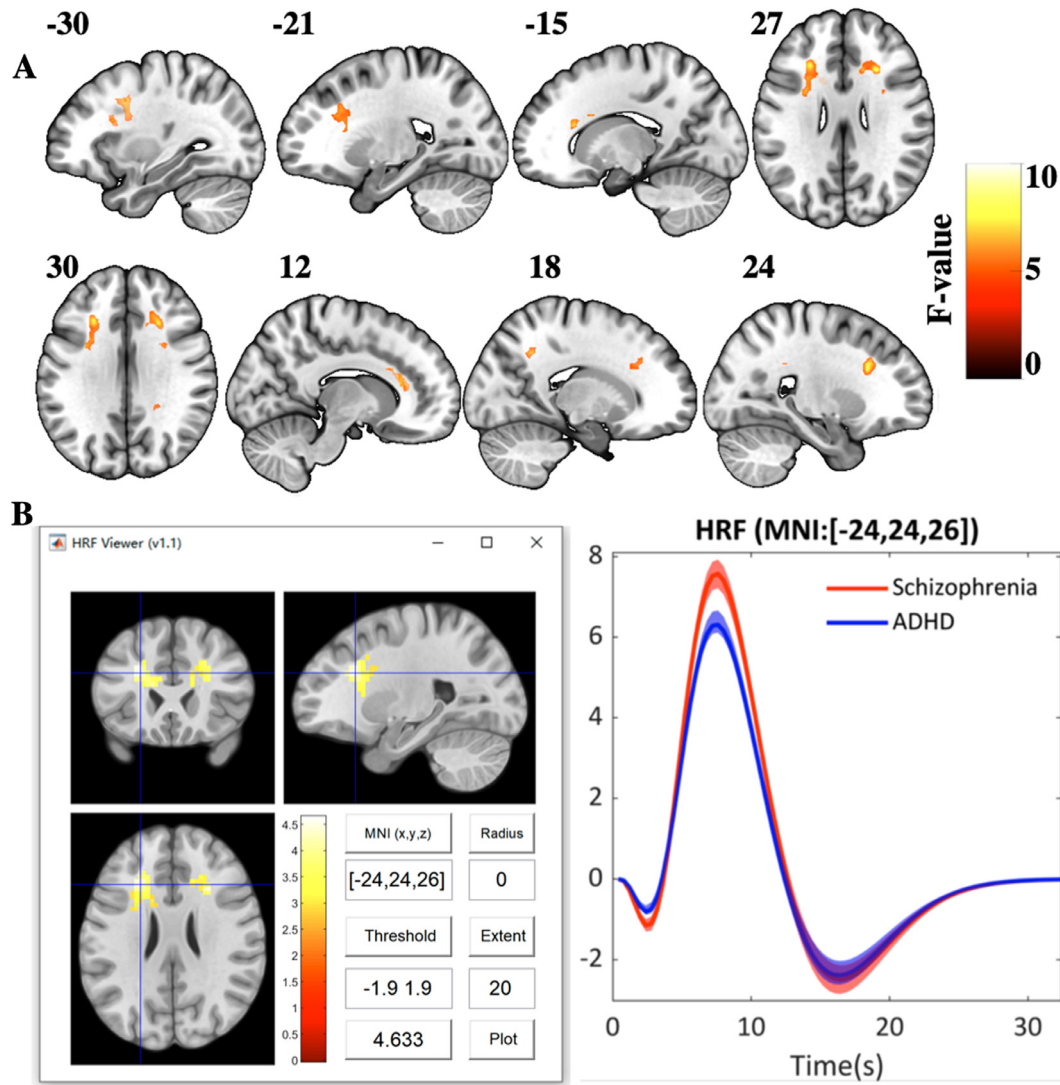


**Fig. 4.** (A) main effect of group.  $p < 0.05$  FDR correction at voxel level, cluster size  $> 20$  voxels. (B) Illustration of rsHRF Viewer graphical interface, left: typical graphical interface after loading the statistical image and HRF mat files; right: the output (mean (solid line) + standard error (shadow)) after clicking 'plot'.

**Table 3**

The model performance of individual age prediction. MAE: mean absolute error.

	BOLD		Deconvolved BOLD	
	$r$	MAE	$r$	MAE
Scanner 1 (n=79)	-0.112( $p=0.737$ )	7.337( $p=0.472$ )	0.269( $p=0.005$ )	6.573( $p=0.003$ )
Scanner 2 (n=20)	0.429( $p=0.006$ )	5.220( $p=0.004$ )	0.784( $p<0.001$ )	3.751( $p<0.001$ )
Model generalization from Scanner 1 to Scanner 2	0.0413( $p=0.386$ )	6.407( $p=0.053$ )	0.364( $p=0.05$ )	11.059( $p=0.884$ )
Model generalization from Scanner 2 to Scanner 1	0.163( $p=0.162$ )	34.817( $p=0.741$ )	0.167 ( $p=0.021$ )	14.895( $p=0.415$ )

**Table 4**

The running time of seven HRF estimation algorithms (input data: 9354 variables with 152 samples). The tests were run on the Dell Precision T1700 with the following specifications: Operating System: Windows 10 Pro 64-bit; Processor: Intel(R) Xeon(R) CPU E3-1240 v3 @ 3.40 GHz, Installed memory (RAM): 32 GB).

Time Taken (s)	Canonical HRF + time derivative	Canonical HRF + time & dispersion derivatives	Gamma functions	Fourier set	Fourier set (Hanning)	FIR	sFIR
Matlab (R2020a)	38.0	43.1	44.8	60.4	59.2	74.3	105.8
Python (3.8.5)	546.7	554.5	557.6	587.9	590.0	607.5	529.0

[https://www.nitrc.org/frs/?group\\_id=1304#](https://www.nitrc.org/frs/?group_id=1304#)). Increasing the number of cores could decrease the computational time.

## 5. Discussion

We introduce a Matlab/Python toolbox for resting-state HRF estimation, deconvolution, and visualization. The toolbox offers both the user-friendly GUI and the command-line option to implement resting-state brain activity and connectivity analysis. The feasibility and effectiveness of the proposed algorithm are validated on the co-localized optical and electrical signals simultaneously recorded from the rat SI under burst-suppression anaesthesia condition. Our results showed that the ground truth HRF can be recovered by blind HRF retrieval algorithms. A publicly available dataset was further employed to demonstrate its functionality. We found that HRF vary across different psychiatric diseases, and hemodynamic deconvolution may improve prediction of age by resting-state FC, which complement the growing evidence for a beneficial effect of HRF deconvolution in resting-state brain connectivity analysis.

We assume that the hemodynamic responses for all spontaneous neural events at all locations in the brain can be represented uniquely as a linear combination of the corresponding basis vectors. The “informed” basis set (canonical HRF with its delay and dispersion derivatives) were employed in previous studies (Wu et al., 2013b, 2019). The HRF can also be reconstructed via FIR (Goutte et al., 2000; Ciuciu et al., 2003) or using ‘selective averaging’ (Dale and Buckner, 1997). The (smooth) FIR model allows us to perform HRF estimation and deconvolution for different imaging techniques (OSI and fMRI) and species (rat and human) (Goutte et al., 2000). However, the FIR model may induce more bias in the recovery of temporal characteristics of HRF (FWHM and T2P) in contrast to the canonical HRF with two derivatives. In our validation experiments, we employed the Gamma functions and Fourier set (Henson and Friston, 2007) as the basis functions to demonstrate the HRF differences across different psychiatric diseases. In addition, the nonparametric impulse response estimation algorithm was also provided in rsHRF (only in Matlab version *rsHRF\_estimation\_impulseest.m*) for regularized estimates of HRF with different regularizing kernels. Our result showed that the nonparametric impulse response function works well in rat IOS. More detailed information of the validity and power of generic HRF models have been explored in previous studies (Lindquist et al., 2009).

Numerous studies have investigated the grey matter HRF characteristics in response to simple or complex tasks. Based on these task HRFs, we are able to assess the contribution of aging, pathologies and genetic factors to HRF variability (Shen et al., 2017; Turner et al., 2019; West et al., 2019). The resting state HRF reduce the complexity of task design and allow us to explore hemodynamic response in special population, such as the unconscious patients (Wu et al., 2019). The surface-based ROIwise HRF difference detected in this study were consistent with previous findings of HRF alteration across different psychiatric diseases (Tamm et al., 2004; Lagopoulos et al., 2007; Mayer et al., 2013). The machine learning results further indicated HRF variability may confound the functional connectome fingerprinting. We cannot find any model generalization capability in the independent sample using the FC model without HRF deconvolution. This also explains that recent finding showed that brain-age prediction is low with the FC model in the large sample dataset (de Lange et al., 2020). Interestingly, the HRF deconvolved data could produce reliable biomarkers for brain-age prediction, even using the features from small sample dataset. Nonetheless, further validation is required with different networks/atlas and large sample dataset, as the accuracy of brain-age prediction may improve with increasing sample size and age range (de Lange et al., 2020). It is also worth to mention that, HRF deconvolution procedure model the autocorrelation of BOLD signal, which may alter the graph theoretical description of human connectome (Afyouni et al., 2019). A recent event-related cognitive task study characterized distinct HRFs profiles in white matter compared to grey matter (Li et al., 2019). Here we estimate the resting state HRF characteristics in white matter for the first time to assess the white matter HRF

variability. Our results indicate HRF alteration across healthy controls and different psychiatric diseases in the genu of corpus callosum and the anterior corona radiata. This is concordant with previous diffusion MRI findings delineate that corpus callosum and anterior corona radiata mal-functioning are always linked with neurodevelopmental and psychiatric disorder (Pavuluri et al., 2009; Davenport et al., 2010; van der Knaap and van der Ham, 2011). In fact, the genu of corpus callosum contains high density of thin myelinated axons which connect the prefrontal cortex and higher order sensory areas. The anterior corona radiata extends from ventrolateral and dorsolateral prefrontal cortex primarily to pre-tectum. The psychiatric disease was associated with disturbances in the prefrontal regions. Resting state HRF can thus provide new insights on the functional architecture of the pathological brain in white matter.

One question that can arise is whether the rsHRF could be used as a proxy of the task-evoked HRF. The rationale would be that one can think of the HRF as a fixed transfer function between neural activity and hemodynamics, and in this sense it should be constant across tasks. Yet increasing evidence points to a variability of the HRF across tasks and conditions (Handwerker et al., 2012; Elbau et al., 2018; Taylor et al., 2018; Cardoso et al., 2019). In this sense we would certainly encourage (and engage ourselves in) more research along these lines, using hierarchical and clustering approaches to find one or more HRFs per voxel and per subject across tasks, but in this paper aimed to present the toolbox itself we did not feel comfortable in proposing the rsHRF as a benchmark or prototype for a universal HRF.

A further aspect complicating this issue is that in the span of a TR, several neural events could happen and potentially overlap. This has been addressed only recently for EEG, and in case of a clear design matrix (Ehinger and Dimigen, 2019), and the approach could be extended to fMRI and to blind detection of pseudoevents.

Then there is the trade-off between assuming that the rsHRF does not change over an acquisition, and thus more events would result in better estimation, or to account for a variability of the rsHRF across the same acquisition. Here we position ourselves in the middle, and go for a “session-specific” rsHRF. The optimal number of events necessary for a stable rsHRF estimation is also a variable quantity depending on the signal to noise ratio (SNR), on possible simultaneous events, of signal variability. Without giving a definitive answer, we have performed simulations on two extreme cases (SNR 0 and SNR 10, *rsHRF\_sim\_events\_CV.m*), obtaining a stabilization in the coefficient of variation after 3 events in the former case, and 16 in the latter.

Finally a word on breath hold paradigms. These protocols have proven extremely useful in calibration of the BOLD signal and the assessment of cerebrovascular reactivity (Murphy et al., 2011; Moia et al., 2020, 2021). By construction the point-process approach on which this toolbox rests, does not apply in breath hold paradigms.

## Credit authorship contribution statement

**Guo-Rong Wu:** Conceptualization, Methodology, Software, Validation, Funding acquisition, Writing – review & editing. **Nigel Colenbier:** Methodology, Software, Validation, Writing – review & editing. **Sofie Van Den Bossche:** Methodology, Software, Validation. **Kenzo Clauw:** Software, Validation. **Amogh Johri:** Software, Validation. **Madhur Tandon:** Software, Validation. **Daniele Marinazzo:** Conceptualization, Methodology, Software, Validation, Funding acquisition, Writing – review & editing.

## Acknowledgments

This work was supported by the National Natural Science Foundation of China (NSFC, grant 61876156 awarded to GW), by the Fund for Scientific Research-Flanders (FWO-V, grant FWO16-ASP-050 awarded to NC, FWO-V, grant G036716N awarded to DM and supporting SvdB), by the European Union's Horizon 2020 Framework Programme for Research and Innovation under the Specific Grant Agreement No. 785907



(Human Brain Project SGA2 awarded to DM and supporting KC), and by Google via the Summer of Code program via the International Neuroinformatics Coordination Facility (MT and AJ).

We thank Wen-Ju Pan and Shella Keilholz for sharing their simultaneous IOS and LFP data, Soichi Hayashi and Franco Pestilli for assistance with inclusion of the toolbox in Brainlife.io, and Asier Erramuzpe Aliaga for co-mentorship of the Google Summer of Code 2018 program.

We thank Rémi Gau for a thorough and illuminating code review, as well as another anonymous reviewer.

## Supplementary materials

Supplementary material associated with this article can be found, in the online version, at [doi:10.1016/j.neuroimage.2021.118591](https://doi.org/10.1016/j.neuroimage.2021.118591).

## References

- Afyouni, S., Smith, S.M., Nichols, T.E., 2019. Effective degrees of freedom of the Pearson's correlation coefficient under autocorrelation. *Neuroimage* 199, 609–625.
- Badillo, S., Vincent, T., Ciuciu, P., 2013. Group-level impacts of within- and between-subject hemodynamic variability in fMRI. *Neuroimage* 82, 433–448.
- Boynton, G.M., Engel, S.A., Heeger, D.J., 2012. Linear systems analysis of the fMRI signal. *Neuroimage* 62 (2), 975–984.
- Buxton, R.B., 2012. Dynamic models of BOLD contrast. *Neuroimage* 62 (2), 953–961.
- Buxton, R.B., Wong, E.C., Frank, L.R., 1998. Dynamics of blood flow and oxygenation changes during brain activation: the balloon model. *Magn. Reson. Med.* 39 (6), 855–864.
- Caballero-Gaudes, C., Moia, S., Panwar, P., Bandettini, P.A., Gonzalez-Castillo, J., 2019. A deconvolution algorithm for multi-echo functional MRI: multi-echo sparse paradigm free mapping. *Neuroimage* 202, 116081.
- Cardoso, M.M.B., Lima, B., Sirotni, Y.B., Das, A., 2019. Task-related hemodynamic responses are modulated by reward and task engagement. *PLoS Biol.* 17 (4), e3000080.
- Chen, G., Saad, Z.S., Adelman, N.E., Leibenluft, E., Cox, R.W., 2015. Detecting the subtle shape differences in hemodynamic responses at the group level. *Front. Neurosci.* 9, 375.
- Ciuciu, P., Poline, J.B., Marrelec, G., Idier, J., Pallier, C., Benali, H., 2003. Unsupervised robust nonparametric estimation of the hemodynamic response function for any fMRI experiment. *IEEE Trans. Med. Imaging* 22 (10), 1235–1251.
- Dale, A.M., Buckner, R.L., 1997. Selective averaging of rapidly presented individual trials using fMRI. *Hum. Brain Mapp.* 5 (5), 329–340.
- Davenport, N.D., Karatekin, C., White, T., Lim, K.O., 2010. Differential fractional anisotropy abnormalities in adolescents with ADHD or schizophrenia. *Psychiatry Res.* 181 (3), 193–198.
- David, O., Guillemain, I., Saillet, S., Rey, S., Deransart, C., Segebarth, C., Depaulis, A., 2008. Identifying neural drivers with functional MRI: an electrophysiological validation. *PLoS Biol.* 6 (12), 2683–2697.
- de Lange, A.G., Anaturk, M., Suri, S., Kaufmann, T., Cole, J.H., Griffanti, L., Zsoldos, E., Jensen, D.E.A., Filippini, N., Singh-Manoux, A., Kivimaki, M., Westlye, L.T., Ebmeier, K.P., 2020. Multimodal brain-age prediction and cardiovascular risk: the Whitehall II MRI sub-study. *Neuroimage* 222, 117292.
- Ehinger, B.V., Dimigen, O., 2019. Unfold: an integrated toolbox for overlap correction, non-linear modeling, and regression-based EEG analysis. *PeerJ* 7, e7838.
- Elbau, I.G., Bruckmeier, B., Uhr, M., Arloth, J., Czamara, D., Spoormaker, V.I., Cizisch, M., Stephan, K.E., Binder, E.B., Samann, P.G., 2018. The brain's hemodynamic response function rapidly changes under acute psychosocial stress in association with genetic and endocrine stress response markers. *Proc. Natl. Acad. Sci. U.S.A.* 115 (43), E10206–E10215.
- Friston, K.J., Mechelli, A., Turner, R., Price, C.J., 2000. Nonlinear responses in fMRI: the Balloon model, Volterra kernels, and other hemodynamics. *Neuroimage* 12 (4), 466–477.
- Gorgolewski, K.J., Durnez, J., Poldrack, R.A., 2017. Preprocessed consortium for neuropsychiatric phenomics dataset. *F1000Res* 6, 1262.
- Goutte, C., Nielsen, F.A., Hansen, L.K., 2000. Modeling the haemodynamic response in fMRI using smooth FIR filters. *IEEE Trans. Med. Imaging* 19 (12), 1188–1201.
- Handwerker, D.A., Gonzalez-Castillo, J., D'Esposito, M., Bandettini, P.A., 2012. The continuing challenge of understanding and modeling hemodynamic variation in fMRI. *Neuroimage* 62 (2), 1017–1023.
- Henson, R., Friston, K., 2007. Convolution models for fMRI. In: *Statistical Parametric Mapping: The Analysis of Functional Brain Images*. Academic Press, pp. 178–192.
- Hiller, A., Chin, R.T., 1991. Iterative Wiener filters for image restoration. *IEEE Trans. Signal Process.* 39, 1892–1899.
- Karahanoglu, F.I., Caballero-Gaudes, C., Lazeyras, F., Van de Ville, D., 2013. Total activation: fMRI deconvolution through spatio-temporal regularization. *Neuroimage* 73, 121–134.
- Keles, H.O., Barbour, R.L., Omurtag, A., 2016. Hemodynamic correlates of spontaneous neural activity measured by human whole-head resting state EEG+fNIRS. *Neuroimage* 138, 76–87.
- Lagopoulos, J., Ivanovski, B., Malhi, G.S., 2007. An event-related functional MRI study of working memory in euthymic bipolar disorder. *J. Psychiatry Neurosci.* 32 (3), 174–184.
- Laird, A.R., Fox, P.M., Eickhoff, S.B., Turner, J.A., Ray, K.L., McKay, D.R., Glahn, D.C., Beckmann, C.F., Smith, S.M., Fox, P.T., 2011. Behavioral interpretations of intrinsic connectivity networks. *J. Cognit. Neurosci.* 23 (12), 4022–4037.
- Li, M., Newton, A.T., Anderson, A.W., Ding, Z., Gore, J.C., 2019. Characterization of the hemodynamic response function in white matter tracts for event-related fMRI. *Nat. Commun.* 10 (1), 1140.
- Lindquist, M.A., Meng Loh, J., Atlas, L.Y., Wager, T.D., 2009. Modeling the hemodynamic response function in fMRI: efficiency, bias and mis-modeling. *Neuroimage* 45 (1 Suppl), S187–S198.
- Lindquist, M.A., Wager, T.D., 2007. Validity and power in hemodynamic response modeling: a comparison study and a new approach. *Hum. Brain Mapp.* 28 (8), 764–784.
- Marinazzo, D., Pellicoro, M., Stramaglia, S., 2012. Causal information approach to partial conditioning in multivariate data sets. *Comput. Math. Methods Med.* 2012, 303601.
- Mayer, A.R., Ruhl, D., Merideth, F., Ling, J., Hanlon, F.M., Bustillo, J., Canive, J., 2013. Functional imaging of the hemodynamic sensory gating response in schizophrenia. *Hum. Brain Mapp.* 34 (9), 2302–2312.
- Miezin, F.M., Maccotta, L., Ollinger, J.M., Petersen, S.E., Buckner, R.L., 2000. Characterizing the hemodynamic response: effects of presentation rate, sampling procedure, and the possibility of ordering brain activity based on relative timing. *Neuroimage* 11 (6 Pt 1), 735–759.
- Moia, S., Stickland, R.C., Ayyagari, A., Termenon, M., Caballero-Gaudes, C., Bright, M.G., 2020. Voxelwise optimization of hemodynamic lags to improve regional CVR estimates in breath-hold fMRI. In: *Proceedings of the Annual International Conference of the IEEE Engineering in Medicine and Biology Society*, 2020, pp. 1489–1492.
- Moia, S., Termenon, M., Urunuela, E., Chen, G., Stickland, R.C., Bright, M.G., Caballero-Gaudes, C., 2021. ICA-based denoising strategies in breath-hold induced cerebrovascular reactivity mapping with multi echo BOLD fMRI. *Neuroimage* 233, 117914.
- Murphy, K., Harris, A.D., Wise, R.G., 2011. Robustly measuring vascular reactivity differences with breath-hold: normalising stimulus-evoked and resting state BOLD fMRI data. *Neuroimage* 54 (1), 369–379.
- Neelamani, R., Choi, H., Baraniuk, R., 2004. ForWaRD: Fourier-wavelet regularized deconvolution for ill-conditioned systems. *IEEE Trans. Signal Process.* 52 (2), 418–433.
- Ng, K.K., Lo, J.C., Lim, J.K.W., Chee, M.W.L., Zhou, J., 2016. Reduced functional segregation between the default mode network and the executive control network in healthy older adults: a longitudinal study. *Neuroimage* 133, 321–330.
- Pan, W.J., Lee, S.Y., Billings, J., Nezafati, M., Majeed, W., Buckley, E., Keilholz, S., 2018. Detection of neural light-scattering activity in vivo: optical transmittance studies in the rat brain. *Neuroimage* 179, 207–214.
- Pavuluri, M.N., Yang, S., Kamineni, K., Passarotti, A.M., Srinivasan, G., Harral, E.M., Sweeney, J.A., Zhou, X.J., 2009. Diffusion tensor imaging study of white matter fiber tracts in pediatric bipolar disorder and attention-deficit/hyperactivity disorder. *Biol. Psychiatry* 65 (7), 586–593.
- Poldrack, R.A., Congdon, E., Triplett, W., Gorgolewski, K.J., Karlsgodt, K.H., Mumford, J.A., Sabb, F.W., Freimer, N.B., London, E.D., Cannon, T.D., Bilder, R.M., 2016. A phenome-wide examination of neural and cognitive function. *Sci. Data* 3, 160110.
- Raichle, M.E., 2011. The restless brain. *Brain Connect.* 1 (1), 3–12.
- Rangaprakash, D., Dretsche, M.N., Yan, W., Katz, J.S., Denney Jr., T.S., Deshpande, G., 2017. Hemodynamic variability in soldiers with trauma: Implications for functional MRI connectivity studies. *Neuroimage Clin.* 16, 409–417.
- Rangaprakash, D., Wu, G.R., Marinazzo, D., Hu, X., Deshpande, G., 2018. Hemodynamic response function (HRF) variability confounds resting-state fMRI functional connectivity. *Magn. Reson. Med.* 80 (4), 1697–1713.
- Seeley, W.W., Menon, V., Schatzberg, A.F., Keller, J., Glover, G.H., Kenna, H., Reiss, A.L., Greicius, M.D., 2007. Dissociable intrinsic connectivity networks for salience processing and executive control. *J. Neurosci.* 27 (9), 2349–2356.
- Shen, X., Finn, E.S., Scheinost, D., Rosenberg, M.D., Chun, M.M., Papademetris, X., Constable, R.T., 2017. Using connectome-based predictive modeling to predict individual behavior from brain connectivity. *Nat. Protoc.* 12 (3), 506–518.
- Tagliazucchi, E., Balenzuela, P., Fraiman, D., Chialvo, D.R., 2012. Criticality in large-scale brain fMRI dynamics unveiled by a novel point process analysis. *Front. Physiol.* 3, 15.
- Tamm, L., Menon, V., Ringel, J., Reiss, A.L., 2004. Event-related fMRI evidence of frontotemporal involvement in aberrant response inhibition and task switching in attention-deficit/hyperactivity disorder. *J. Am. Acad. Child Adolesc. Psychiatry* 43 (11), 1430–1440.
- Taylor, A.J., Kim, J.H., Ress, D., 2018. Characterization of the hemodynamic response function across the majority of human cerebral cortex. *Neuroimage* 173, 322–331.
- Tipping, M.E., 2001. Sparse Bayesian learning and the relevance vector machine. *J. Mach. Learn. Res.* 1 (Jun), 211–244.
- Turner, M.P., Hubbard, N.A., Sivakolundu, D.K., Himes, L.M., Hutchison, J.L., Hart Jr., J., Spence, J.S., Frohman, E.M., Frohman, T.C., Okuda, D.T., Rypma, B., 2019. Preserved canonicity of the BOLD hemodynamic response reflects healthy cognition: insights into the healthy brain through the window of Multiple Sclerosis. *Neuroimage* 190, 46–55.
- van der Knaap, L.J., van der Ham, I.J., 2011. How does the corpus callosum mediate interhemispheric transfer? A review. *Behav. Brain Res.* 223 (1), 211–221.
- Van Essen, D.C., Smith, S.M., Barch, D.M., Behrens, T.E., Yacoub, E., Ugurbil, K. The WU-Minn HCP Consortium, 2013. The WU-Minn human connectome project: an overview. *Neuroimage* 80, 62–79.
- West, K.L., Zupichini, M.D., Turner, M.P., Sivakolundu, D.K., Zhao, Y., Abdelkarim, D., Spence, J.S., Rypma, B., 2019. BOLD hemodynamic response function changes significantly with healthy aging. *Neuroimage* 188, 198–207.
- Wu, G.R., Di Perri, C., Charland-Verville, V., Martial, C., Carriere, M., Vanhauzenhuyse, A., Laureys, S., Marinazzo, D., 2019. Modulation of the spontaneous hemodynamic response function across levels of consciousness. *Neuroimage* 200, 450–459.
- Wu, G.R., Liao, W., Stramaglia, S., Chen, H., Marinazzo, D., 2013a. Recovering directed



- networks in neuroimaging datasets using partially conditioned Granger causality. *Brain Connect.* 3 (3), 294–301.
- Wu, G.R., Liao, W., Stramaglia, S., Ding, J.R., Chen, H., Marinazzo, D., 2013b. A blind deconvolution approach to recover effective connectivity brain networks from resting state fMRI data. *Med. Image Anal.* 17 (3), 365–374.
- Wu, G.R., Marinazzo, D., 2015. Point-process deconvolution of fMRI BOLD signal reveals effective connectivity alterations in chronic pain patients. *Brain Topogr.* 28 (4), 541–547.
- Wu, G.R., Marinazzo, D., 2016. Sensitivity of the resting-state haemodynamic response function estimation to autonomic nervous system fluctuations. *Philos. Trans. A Math. Phys. Eng. Sci.* 374 (2067).
- Yan, W., Rangaprakash, D., Deshpande, G., 2018. Aberrant hemodynamic responses in autism: implications for resting state fMRI functional connectivity studies. *Neuroimage Clin.* 19, 320–330.
- Yeo, B.T., Krienen, F.M., Sepulcre, J., Sabuncu, M.R., Lashkari, D., Hollinshead, M., Roffman, J.L., Smoller, J.W., Zollei, L., Polimeni, J.R., Fischl, B., Liu, H., Buckner, R.L., 2011. The organization of the human cerebral cortex estimated by intrinsic functional connectivity. *J. Neurophysiol.* 106 (3), 1125–1165.
- Zhang, D., Raichle, M.E., 2010. Disease and the brain's dark energy. *Nat. Rev. Neurol.* 6 (1), 15–28.